Fall 2021

Increased Detectivity and Low Temperature Performance Analysis of Sub-20μm Micropixel Array A1GaN UV Photodiodes

Samia Islam

INCREASED DETECTIVITY AND LOW TEMPERATURE PERFORMANCE ANALYSIS OF SUB-20μm MICROPIXEL ARRAY AlGaN UV PHOTODIODES

by

Samia Islam

Bachelor of Science
University of Dhaka, 2015

Master of science
University of Dhaka, 2017

Submitted in Partial Fulfillment of the Requirements

For the Degree of Master of Science in

Electrical Engineering

University of South Carolina

2022

Accepted by:

MVS Chandrasekhar, Major Professor

Asif Khan, Reader

Tracey L. Weldon, Interim Vice Provost and Dean of the Graduate School

ACKNOWLEDGEMENTS

First, I would like to thank my family, friends, and all my colleagues for their enormous support. I am gratified to all my family members for understanding me during my hard times and making my journey easier than my expectation.

Special thanks to my advisor Dr. Chandra for guiding me throughout this whole journey. Dr. Asif khan has given me an opportunity to work in his lab and I can't be enough thankful for that. His lab provides me with all the necessary facilities to conduct my research in such a nice environment.

I sincerely appreciate the time and effort that Richard, Shahab, and Dr. Gaevski put in to ensure that I can finish my thesis. They were always there whenever I need any kind of help regarding my research. I cannot express how grateful I am to have them as my mentors. The skills that they taught me surely helped me a lot to conduct all my experiments properly and efficiently.

Last but not the least, I would like to thank my husband Tahmid for supporting me throughout my whole journey. After my parents, he is the one who kept faith in me all the time. I just want to appreciate everything he did for me and be there always when I needed him most.

ABSTRACT

This thesis is divided into two sections. At first, we demonstrate ~1.5x detectivity increase in AlGaN photodiodes on sapphire using distributed micropixel arrays with 5-15 μm pixel diameter. This is due to the ~10x larger chip footprint of the 5um diameter micropixel arrays compared to planar control structures with identical p contact area. The responsivity of the larger areas was the same as that of the control structure despite the larger footprint while the dark currents, an indicator of noise, remained unchanged. The photocurrent generated between pixels was collected due to transmission line effects connecting the pixels separated by 5um, rather than minority carrier diffusion alone, which would fall off at <1um. The limiting factor is how far apart the micropixels can be separated, determined by the transfer length in the n+ AlGaN contact formation layer, in turn a strong function of photocurrent magnitude.

In the second section, we have analyzed low temperature performances of these photodiodes. Measured I-Vs at different temperature (90K-300K) ranges do show some shift in turn on voltage and current magnitude. Using MATLAB, we verified two different circuit models which can correctly predict the nano pipe freeze out mechanism at lower temperatures and explained the reason behind the 4x increase of light intensity.

TABLE OF CONTENTS

LIST OF TABLES

LIST OF FIGURES

Figure 4.13 Average Photocurrent for 6 scanned lines 47

LIST OF ABBREVIATIONS

DUV ..... Deep Ultraviolet

AlGaN ..... Aluminum Gallium Nitride

AlN ..... Aluminum Nitride

MQW ..... Multiple Quantum Well

GaN ..... Gallium Nitride

EQE ..... External Quantum Efficiency

MOCVD ..... Metal Organic Chemical Vapor Deposition

LED ..... Light Emitting Diode

PD ..... Photo Detector

CHAPTER 1

INTRODUCTION

"It was at Bell Labs that I first made direct contact with real semiconductor experts and thus began to fully understand what amazing materials they were and what they could do".

Robert B. Laughlin

Modern semiconductor technologies undeniably hold the potential to revolutionize the optoelectronics world in much the similar way as the invention of the silicon (Si) chip over 50 years ago enabled the modern computer era. At the center of the technologies are the physical characteristics of the semiconductor materials themselves: that enable electrons, holes, and photons to interact and control each other in a wide variety of device architectures. As a result, the optoelectronics field is undergoing a rapid change with the introduction of wide-bandgap (WBG) semiconductors. Nowadays benefiting from the progress of these materials, light sensing technology is hailed with significant uprisings. Some of the unique features of photodetectors such as high sensitivity, reliability, ease of use, linearity and high spectral selectivity have been accomplished after more than a century's steady development [1].

Inspired by Einstein's revolutionary explanation of photoelectric effect, transforming photons into electrical signal were subsequently developed which is the main foundation of modern photosensor devices. A technology roadmap of these developments has been shown in Figure 1.1.

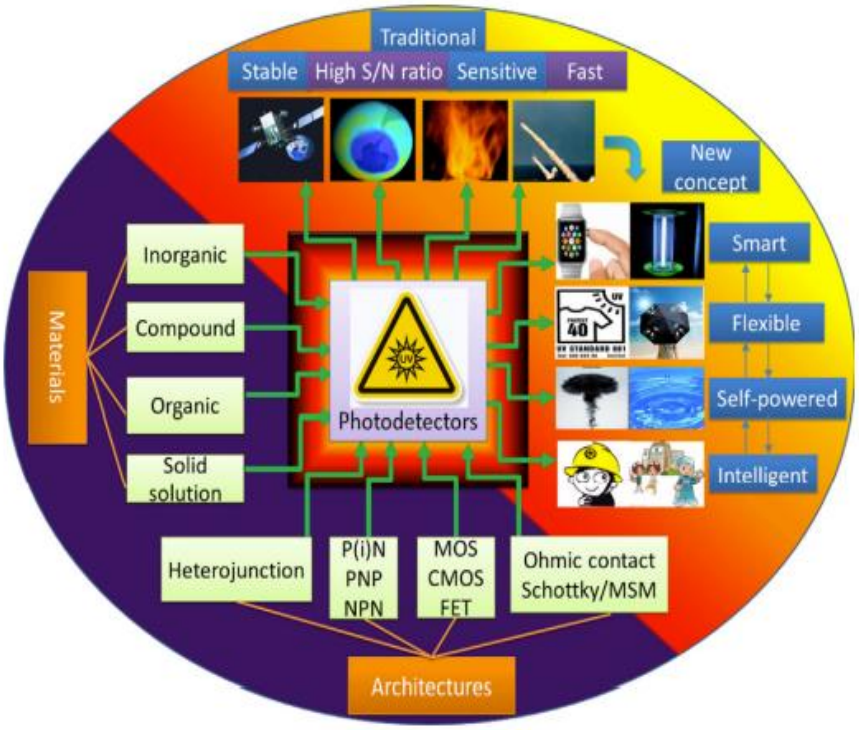

Figure 1.1: An Overview of the next generational chip scale photodetectors [2].

Nowadays as intensified UV radiation has become more alarming, UV photodetection has drawn considerable attention from scientists in the relevant field. The international commission on illumination (CIE) has divided the UV light into four spectral regions: UV-A (for wavelengths from 400 to 320 nm), UV-B (for wavelengths from 320 to 280 nm), UV-C (for wavelengths from 280 to 200 nm), and far UV (for wavelength

between 200 to10 nm), which reaches the X-ray spectral low energy frontier) [3-5]. An outline of solar spectrum has been demonstrated in figure 1.2.

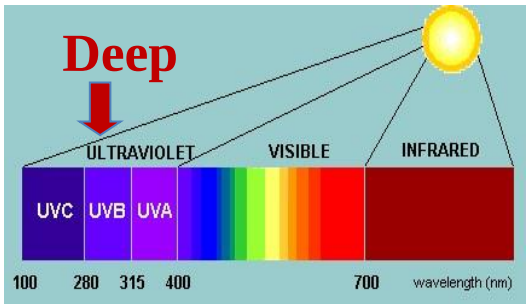

Figure 1.2: Sunlight and Solar Spectrum.

It is revealed from the ongoing research that a decline of 1% in the volume of the ozone layer will cause an increase of 2% in UV radiation at ground level, which will significantly increase the incident rate of skin cancer [2]. Moreover, it is also found that ultraviolet radiation has a statistically significant effect on daily COVID-19 growth rates. So, detection of UV light has become one of the highest priorities in recent days.

However, there are some limitations inherent to the semiconductor material when it comes to detecting or producing light. For manufacturing an ideal device for detection, we must keep in mind that the desired wavelength has higher absorption within the material whereas any wavelength below or above will be transmitted, reflected, or scattered without any contribution. The performance of the photodetector device is hindered mostly if any involvement has been made from the wavelength beyond the desired limit. The peak photo response of the material is directly related to the finite bandgap resulting from the crystalline structure and composition of the material. If incoming photons have energy below this bandgap, no electrons will be excited to conduction band creating electron-hole

pairs for sensing applications. Additionally, if the device is irradiated with photons above bandgap energies, electron hole pairs with additional kinetic energy will be generated and that energy will be distributed throughout the semiconductor as thermal energy. This added energy will increase the noise level which will in turn make it more difficult to accurately detect the required wavelength at low power. This bandgap issue has become a very complex problem as the modern era demands improved sensing of a wider bandwidth of radiation.

The major portion of the photodetector market is currently operated by silicon (C-MOS-based) photodetectors in view of their low cost, high performance, and high integration with electronics. But when it is required to detect UV radiation, The well-established Si technology has some shortcomings because of its band gap energy constrain of 1.1 eV. Costly high pass optical filters and phosphors are therefore required to prevent low energy photons. Thus, the device performance is reduced with temperature, as supported by increasing dark currents. Moreover, Si is an indirect bandgap material which means it has a lower absorption coefficient. So, the detection device made up of silicon will require thicker absorber material layers for higher absorption (10s of μm). Furthermore, while dealing with the C-MOS based Si sensors, we must keep in mind that relatively lower operating speed will hinder our device performance.

To trade with the potential limit of Si sensors, we must replace them with potential materials which have distinct and measurable advantages over the current market leader. Group-III nitrides (AlN, GaN, InN, and their ternary and quaternary compounds) can tune their bandgap up to 6.2 eV which can provide the full UV region photodetection. The improvement of wide-bandgap-semiconductor UV detectors such as GaN, diamond, or

SiC-based systems have therefore arisen, which do not necessitate the insertion of filters, showing their potential for high-temperature applications [6–8]. Table 1.1 provides us with the basic parameters of some common WBG semiconductors that are used during the fabrication of photodetectors.

Table 1.1 Basic parameters of Semiconductors used in UV photodiodes [9]

	Si	GaAs	4H-SiC	Diamond	GaN	AlN
Bandgap E_g (eV)	1.12	1.43 Direct	3.2	5.5	3.39 Direct	6.2 Direct
Thermal Conductivity (W cm^{-1} K^{-1})	1.5	0.5	4.9	20	1.3	3.19
Melting point (K)	1683	1513	2830	3773	2773	2473
Electron Saturation Velocity (10^7cm s^{-1})	1	2	2	2.7	2.5	1.4
Mobility ($cm^2V^{-1}s^{-1}$) Electrons	1400	8500	950	2200	1000	135
Holes	600	400	120	1600	30	14
Dielectric Constant	11.8	12.5	9.7	5.5	8.9	8.5
Breakdown field (10^5 V cm^{-1})	3	6	20	100	26	20

Photodetectors based on WBG semiconductors can surmount many of the challenges possessed by well-established Si technology. Table 1.1 surely provides us with significant statistics to prove the fact that semiconductors with larger bandgap have considerably higher thermal conductivity compared to Si which makes them more suitable for high power and high temperature operation. Bandgap itself is an outstanding advantage as it provides room temperature operation and intrinsic radiation hardness. For example, the widely used Baliga's figure of merit (BFOM) contour can be used to get right research direction towards designing high performance UV sensors.

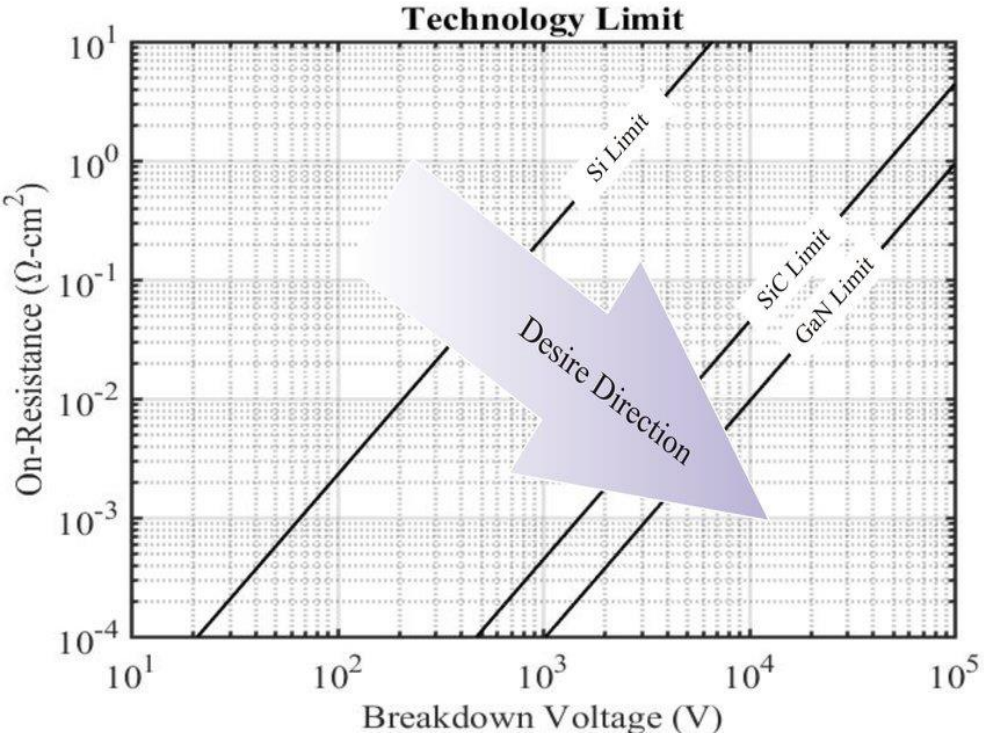

Figure 1.3: Log-log specific on resistance versus breakdown voltage plot

First GaN based detector was implemented by Khan et. al. where two metals were deposited onto the GaN flim for ohmic contact [10]. The main shortcoming was higher

leakage current and failure of performing complete solar blind detection. In 2011, Razeghi summarized the developments of III-nitride materials and amongst them, AlGaN alloys play a significant role in the development of LEDs, avalanche photodiodes (APDs) and photodetectors [11]. In the beginning, the devices were composed of GaN and low Al content AlGaN as high aluminum content device fabrication had always been considered a serious problem. Although the fabrication techniques of UV photodiodes are relatively mature now, due to uniformity problems in material and devices, AlGaN based solar blind detection technology needs to be further improved.

The main constrain of performing UV detection is the epitaxy of high Al content AlGaN alloys with higher crystal quality. Moreover, due to the low p-type doping efficacy of AlGaN [12] it is difficult to get high doping efficiency and high conductivity p- AlGaN materials. Despite material issues, device design must be considered an important influence in the development of solar blind UV sensor technology. Due to a huge number of defects, the photoconductive effect on AlGaN alloy is associated with slow operating speed, sluggish energy photon response and severe temperature dependence. Additionally, there is a tradeoff between the device's operating speed and gain. Researchers are working relentlessly to improve important characteristics such as drift, diffusion, and generation of carriers around the junction to advance the adoption of these devices in the industry.

The main objectives of our research are to compute and study the effects of micropixel based geometry on AlGaN photodiodes using forward, dark, and illuminated current-voltage, photo-responsivity, scanning photocurrent microscopy (SPCM) to compute illuminated current decay length and scanning electron microscopic (SEM)

imaging. The results of this study will hopefully be improvements towards more successful solar blind UV detection and reliably predict the device performance.

The device presented in this study is relatively well-known and understood AlGaN photodiodes on sapphire using distributed micropixel arrays with 5-15um pixel diameter. Compared to planar structure, these arrays have identical p-n diode junction area but a much larger chip footprint area. However, the dark current, which is an indicator of noise remains unchanged despite using a larger footprint. The reasoning behind using this pixel-based geometry is that, if we cover the whole area with smaller micropixels, we are basically preventing a huge number of defects generation by avoiding one gigantic mesa on top of the n+ AlGaN layer. Minimizing defects will help us downscaling leakage current as well as our junction capacitance. Now that as our junction capacitance gets smaller, the speed of the detector will go up. As a result, without compromising all the benefits that a high-speed detector can offer, we can surely provide better photodetection with our device architecture.

For designing the detector, one more thing that should be kept in mind that how far apart we can place these pixels. The transfer length or we can say the decay length of photocurrent in the n+ AlGaN contact formation layer will help us in this regard. In our device, the distance between two adjacent pixels is about 5 μm. Logically the charges cannot be collected only due to diffusion length which will fall off at less than 1 μm. There must be an increasing series resistance for excitation further away from the mesa. Thus, a transmission line model (TLM) is applied to describe the equivalent circuit. So, this novel device architecture can be very promising advancement to current technologies that are

only getting closer to adoption as researchers continue to expand and experiment with their design and product.

CHAPTER 2

MATERIALS AND METHODS

While fabricating our device we have selected Group-III nitrides (AlN, GaN and their ternary and quaternary compounds) as they are a strategic technology for the development of high-performance UV photodetectors. The wide bandgap itself provides an important benefit for photodetectors since it enables room-temperature operation and intrinsic visible-blindness. Moreover, the elevated chemical and thermal stability of GaN-based detectors have progressively attracted fundamental research interest in high-temperature and high photon energy detection. Fig 2.1 surely provided us with sufficient information about optimum Al mole fraction which played a very important role whilst designing our device.

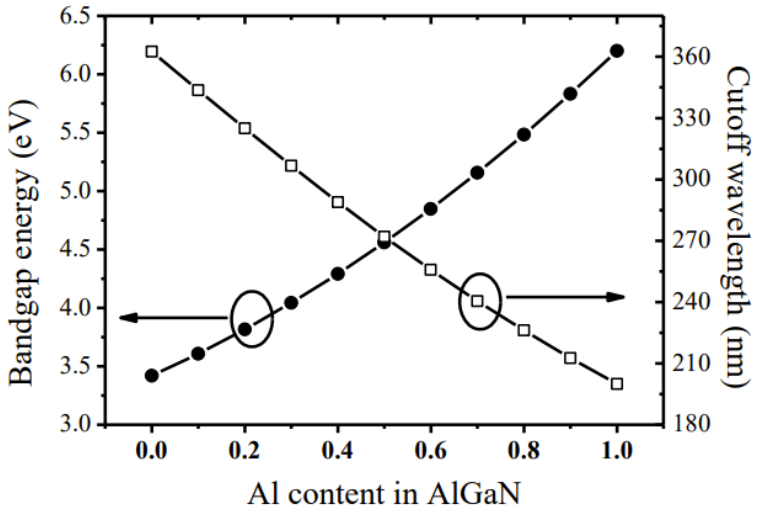

Figure 2.1: Bandgap and cutoff wavelength of AlGaN [13]

As can be seen from the figure, to understand solar-blind detection, the Al composition in $Al_xGa_{1-x}N$ should be higher than 40%. We also knew the fact that for better performance, high-quality AlGaN films must be obtained along with the higher composition of Al. Contrasted to GaN, the growth of AlGaN especially with a high Al composition has proved to be significantly difficult, which lies in the lower migration of Al atoms than that of Ga atoms, and intense parasitic reactions [13]. Therefore, the layer-by-layer growth with the atomic steps on the surface for the films is difficult to accomplish. Dislocations, grain boundaries, stacking faults and other high-density defects are much easier to produce. [14]. As history indicates that to avoid the cracks and absorption losses, AlN is the best choice as a template. Besides taking AlN as a template, improvement of the quality of AlGaN films was also one of our top priorities during fabrication. However, another important fact is that while choosing metal, we should be careful enough to obtain sufficient optical absorption. Thin metals often lead to higher leakage current and are not uniform as well. Back-illumination process can overcome these drawbacks to some extent. Additionally, the amount of nonradiative defects is itself a strong function of the buffer and the active layer's material quality.

2.1 DEVICE FABRICATION

In this report, we have chosen 280 nm emission deep UV LED for our experiment with a layout using $Al_xGa_{1-x}N$ multiple quantum wells ~MQWs in the active region. This design results in a more efficient carrier confinement, and thereby reduces the long-wavelength emission band. To avoid absorption from GaN template, the epilayer structure was grown over 3 μm thick thermally conductive AlN templates over c-plane sapphire

substrates using metalorganic chemical vapor deposition [15]. The epilayer structure of the device of this study is shown in Fig 2.2.

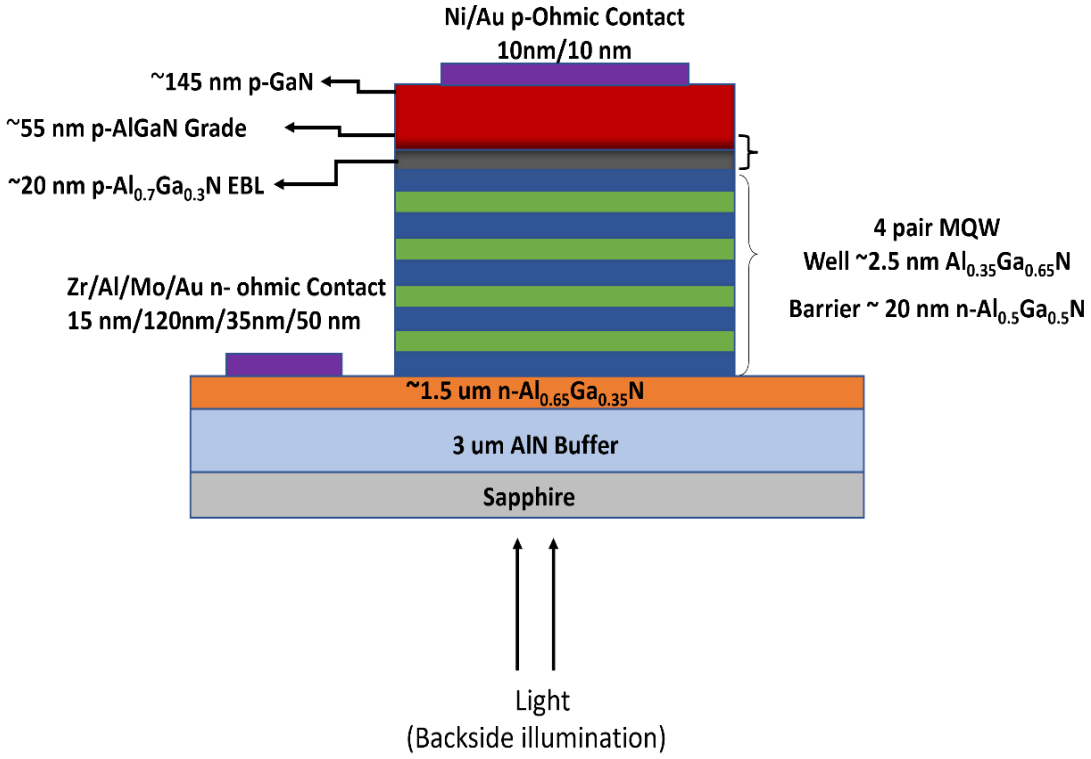

Figure 2.2: Structural Details of micropixel Array Photodiode

The device fabrication procedure consisted of first using a Cl_2/Ar chemistry inductively coupled plasma reactive ion etching (ICP-RIE) to describe the micropixels and access the n-contact making n+-$Al_{0.65}Ga_{0.35}N$ layer [16]. Annealing in a nitrogen environment was then completed at 750 °C to activate the Mg-dopants. Then a narrow picture frame n-contact (5 μm wide) was fabricated around single pixels (for standalone devices) and the subarrays of pixels (for interconnected devices). The n contact metal stack Zr(150 Å)/Al(1200 Å)/Mo(350 Å)/Au (500 Å) was deposited via e-beam and annealed at

950 °C for 3 min in forming gas by rapid thermal annealing (RTA). The internal dimension of this n-contact border was for all cases < 100 μm. We have used this geometry to avoid lateral current crowding [17].

From the n-contact TLM measurements, the sheet resistance for the epilayer structure and the contact resistance was Rsh=120 Ω/sq and $\rho c = 6 \times 10^{-4}$ Ω·cm^2 [16]. Following the n-contact, Ni/Au p contacts were formed over the individual micropixels and annealed at 500°C for 5 min on a hotplate in an O_2 environment. The p-metal measurements were 5, 10 and 15 μm diameter for the micropixels. The first micropixel interconnection stage began with atomic layer deposition (ALD) of a conformal 75 nm thick Al_2O_3 film. Windows above the p-contact regions of the individual micropixels were then opened by ICP-RIE with a high-power $Cl_2/BCl_3/Ar$ based etch. This was followed by photoresist masking and electron-beam deposition of a 300 nm thick reflective aluminum heat-spreader to interconnect the individual micropixels thereby forming the subarrays. The Al interconnect blanketed the entire internal area of the n-ohmic picture frame borders. The second stage of interconnection began with plasma enhanced chemical vapor deposited SiO_2 (400 nm) followed by an $SF_6/CF_3H/Ar$ dry etching with RIE to open windows for each of the subarrays. The final metal stack deposition blanketed and interconnected the 3 × 3 arrays of subarrays.

Here we have explored a new interconnected micropixel design where individual pixels are not connected through the blanket n contact network rather a narrow picture frame border around a densely packed subarrays are formed to increase the active area coverage. This unique design also passivates the pixel sidewalls and spreads the self-generated heat away from the individual pixel. The total fabrication procedure has been

conducted in our lab. Device geometries are schematically shown in Fig 2.3 and table 1 summarizes details for the various device geometries shown in the figure.

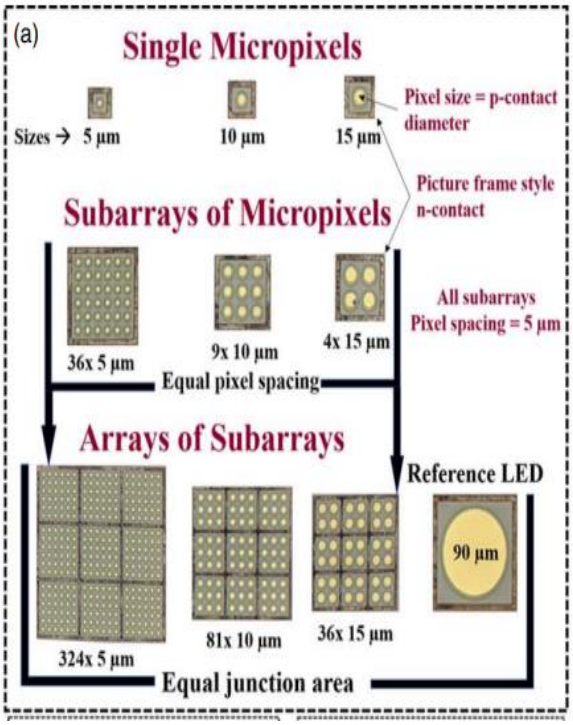

Figure 2.3: Layout of the Device of study

Table 2.1: Device Geometry

Pixel Size	**Pixels per array**	**Junction Area (cm^2)**	**Chip Footprint area (cm^2)**
5 µm	324	$(4.5\ \mu m)^2$ x 3.14 = 1.2e-6	296 µm x 296 µm = 9e-4
10 µm	81	$(7.5\ \mu m)^2$ x 3.14 = 3.53e-6	230 µm x 230 µm = 5e-4
15 µm	36	$(10\ \mu m)^2$ x 3.14 = 6e-6	196 µm x196 µm = 3e-4
90 µm	Reference	$(48\ \mu m)^2$ x 3.14 = 144e-6	129 µm x 129 µm = 1e-4

2.2 EXPERIMENTAL METHODS

Manufactured devices are then electrically characterized by current-voltage (I-V) techniques. The dark I-V data was obtained by conducting forward and reverse bias voltage sweeps, using a Keithley 2612A SMU as the voltage source, on a single standalone device (90 μm) as well as on all the arrays of subarrays. The characteristics acquired from these sweeps were the diode ideality factor (n), reverse saturation current (Is), series resistance (Rs) and shunt resistance (Rsh). The I-V data for the devices under forward bias have been plotted on a semi logarithmic graph. In the near zero turn-on section of the I-V data, the shunt resistance was calculated with a linear curve fit in the positive 0 V region. The series resistance of the device was calculated likewise but within a higher voltage range well after the turn-on of the device. These dark I-V characteristics were the key factors used to understand the initial leakage behavior of micropixel geometry. Equation 2.1 explains the relationship between these parameters.

$$\mathrm{I} = I_s(\mathrm{e}^{\mathrm{qVd/nkT}} - 1) \tag{2.1}$$

Illuminated I-V behavior was one of the principal measurements used to observe fluctuations in the device's actions. The devices were illuminated from the backside by a Cornerstone 1/8m monochromator sourced from a Xenon arc lamp housed in a Thermo Oriel 66902. I-Vs were taken by varying wavelengths under both forward and reverse bias with magnitudes ranging from 0 to 10 V using the same Keithley SMU. For measuring the responsivity, we have chosen -2, -5 and -10 V reverse bias as we know that responsivity can be plotted at any voltage. Although -2 V reverse bias was used to measure detectivity with the application of a photodiode in mind. Generally, the responsivity (A/W) is

calculated by dividing the photocurrent by the incident illumination power of an irradiated device. The photocurrent is defined as the difference between the illuminated current and dark current. The additional current due to the incident light has been used for measuring the responsivity in our report. The irradiance of the monochromator was measured using a Thor Labs C-series Si photodiode (S130C).

Furthermore, 1D Poisson software has been used to plot the band diagram of our structure. This software uses the method of finite differences to find the one-dimensional band diagram of a semiconductor structure. It can automatically calculate the band diagrams for multiple bias voltages. This program simply finds a solution to Poisson's and Schrödinger's equations and generates a complete band diagram of the given epilayer structure.

We have also investigated the devices by scanning the surface with a focused beam of electron. We know that generally in cathodoluminescence, the emission of light has been recorded when atoms excited by high-energy electrons return to their ground state. In our study, we have scanned the devices at different accelerating voltages (5,10 and 20 V) to excite the atoms. CL detectors can analyze the wavelengths emitted by the specimen and display an emission as well as an image of the distribution of cathodoluminescence emitted by the device of study. Imaging has been recorded both at SEI and AUX mode.

Lastly, scanning photocurrent microscopy (SPCM) was employed as a method of spatially mapping the device's illuminated current behavior. A single standalone device was probed and biased according to the configuration in Fig. 2.4. The framework for the SPCM measurement applied a 444 nm laser with a power of roughly 400 µW chopped at 17 Hz as the sample illuminating source as well as the reference signal for the SRS 830 lock-in

amplifier measurements of the current under illumination. SPCM is a technique that uses a raster-scanned local excitation spot to identify spatial alterations in photocurrents, which can be used to recognize localized defects and examine characteristic length scales for carrier transport devices. SPCM has become known as a valuable tool for functional imaging of optoelectronic materials [18], such as semiconductor nanowires [19], solar cells etc. These measurements were performed at no bias and changing forward and reverse biases. It generated spatially resolved X, Y, and phase components of the measured current that were combined to produce the illuminated current in phasor notation for analysis.

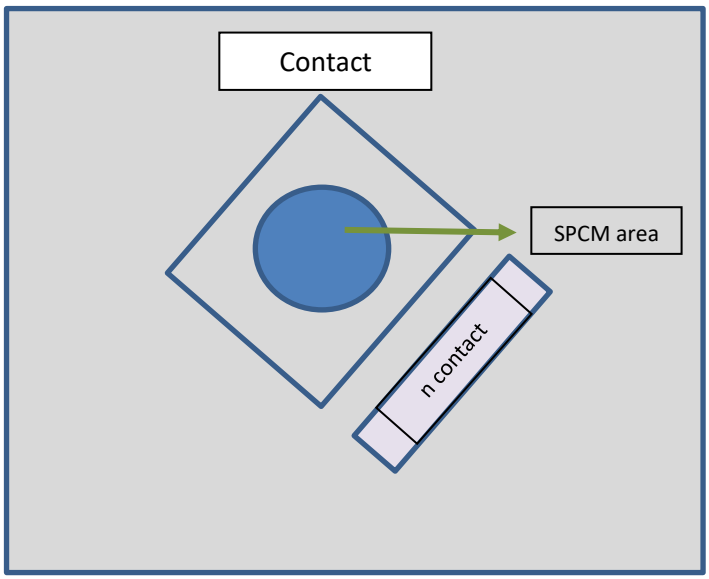

Figure 2.4: Standalone Device and SPCM schematic

Another investigation we have done is by examining the forward I-Vs of our structure at various temperatures. By building an equivalent circuit model we tried to demonstrate the device's internal behavior. We used MATLAB code to simulate the forward current-voltage characteristic of our device. Generally, to simulate the circuit,

SPICE modeling has been preferred. We have used MATLAB for the ease of our computation and, it's less time consuming. Nowadays it is accepted that many of its toolboxes can replace traditional instruments used in advanced electrical engineering applications (SPICE). It is a very widely used tool for electrical engineers.

CHAPTER 3

CURRENT CONDUCTION MECHANISM MODELING OF MICROPIXEL PHOTODIODES

It is a very known fact that, DUV photodiodes possess very massive heating issue. As Most of the commercially used photodiodes are fabricated on sapphire substrate and this substrate has a poor thermal conductivity, self-heating effect is the primary cause of power saturation. Additionally, DUV photons are easily absorbed by the absorptive p-GaN layer and the metal contact in the way of free carrier absorption, which further boosts the self-heating effect for DUV LEDs. Even the flip-chip packaged devices undergo a steady-state temperature rise to about 70 °C at a dc pump current of only 50 mA (at 8 V) resulting in a significant decrease in photodiode output [19]. All these things make the thermal management very important. This chapter briefs readers on predicting the underlying circuit model of these diodes for better thermal management.

For improved management of heat production, not only a clear understanding about device's working principle is very crucial but also one should be aware of the parameters that may affect the performance of optoelectronic devices. Open-core threading dislocations have been shown to limit the performance by functioning as sites of electrical current leakage [20]. These defects are also known as "nanopipes". They can be described as hollow tubes with (10-10) facets.

Nano pipes can be detected through atomic force microscopy, (AFM), conductive AFM (CAFM), transmission electron microscopy (TEM), and even optical microscopy. The electrical current transport through these dislocations can be affected by the density of defects. In another word we can say that the number of nanopipes in a sample determines the current transfer mechanism. At lower temperature, these nano-pipes generally freeze out and I-Vs at different temperatures may seem different because of this "freeze out" effect. Michael *et al.* from Sandia national lab investigated this effect and measured forward-bias current-voltage (IV) responses of two distinct LEDs (DUV-LEDs A and B) with different nanopipe densities [21]. Figure 3.1 represents the result they have observed.

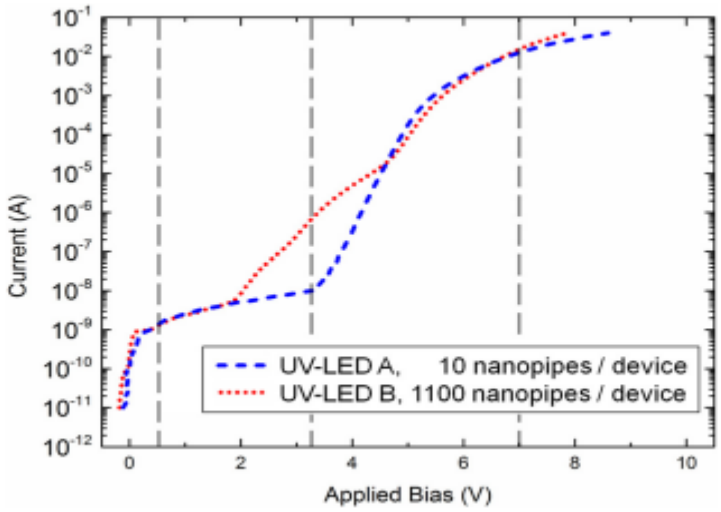

Figure 3.1: Forward I-V characteristics of two LEDs with different defect density

Their 1st device (UV-LED A) had 10 nanopipes and 2nd device had 1100 nanopipe defects per 300 µm*300 µm device. They observed DUV-LED B exhibited an effectively lower turn on voltage of 2 V (versus 3.25 V for DUV-LED A), and up to two orders of magnitude larger current between 2 V and 4.5 V of applied bias. From their study they

came up with a conclusion that the devices with variable defect density need different circuits to explain the conduction mechanism. One circuit model may not be enough for clearer elucidation. For modeling the I-Vs, they used LTspice and all the measurements were done at room temperature.

We used a slightly different approach while deriving the circuit model. For reference we have taken I-Vs of previously mentioned photodiode structure at different temperatures captured by one of my colleagues. It was taken on a packaged device as low temperature measurement could not be done in cryocooler without packaging. For creating a vacuum inside cryocooler he closed the cryostat properly and waited until the vacuum pressure reaches to 20 mTorr. In his EL measurement he found a peak intensity increase by a factor of 4 at lower temperature [22]. The I-V characteristics are plotted on a semilogarithmic scale in the following figure.

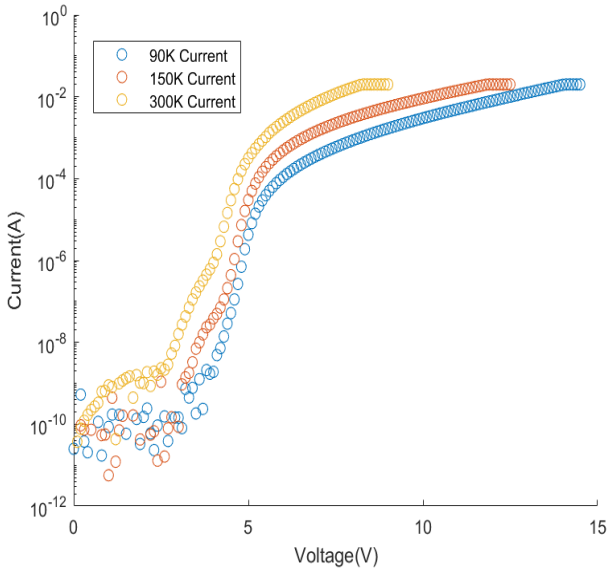

Figure 3.2: I-Vs at different temperature

If we carefully examine the above plot, the structure exhibits a lower turn on voltage of 2.5 V at 300 K (Room temperature) versus 3.9 V at 90 K. The turn on voltage in case of temperature 150 K lies in between the above two temperatures. Similarly, up to two order magnitude of higher current has been spotted at 300 K temperature compared to current at 90 K when bias is applied between 2.5 V to 5 V. The shunt resistance is almost same for all temperatures. Similar results we have observed when a team from Sandia made comparison between two structures with different defect densities. According to them open core threading dislocation provides a low turn on leakage pathway. Leakage diode has lower turn on voltage and decreased amount of shunt resistance. So, although the current value is higher at room temperature for same amount of applied bias, the intensity is lower as light generation normally starts when carriers are recombined at MQW region. In other word when MQW diode starts to conduct, production of light takes place.

Keeping our experimental results on mind we have tried to create a circuit model to predict the underlying conduction mechanism. From the nature of I-Vs, it is quite clear that the density of defects per device is not same at all temperatures. It is a known fact that at lower temperature, nano pipe defects freeze out. When a leakage diode at higher temperature provides an alternative current, in turns it reduces the number of carriers flowing through the MQW-diode path. This alternative current pathway reduces the turn on voltage and shunt resistance. Another important parameter that is affected by defect density is the ideality factor of a diode which is defined as how closely the diode follows ideal diode equation. The ideality factor of the diode is determined from the slope of the forward bias current (ln(I)) versus voltage plot. Due to the worsening of metallic contacts and their interfaces because of temperature reduction, the ideality factor of the diode gets

affected as well. Inspired by all the findings that we got from our experimental result, we tried implementing a modified circuit model which is simpler than the model used by Sandia team. We used two diodes to predict conduction mechanism where diffusion diode is ideality 1 diode and defect diode is the one with ideality 2. Schottky contact is designated by another reverse bias diode. We used MATLAB here to vary the current and calculated the voltage drop across the junction.

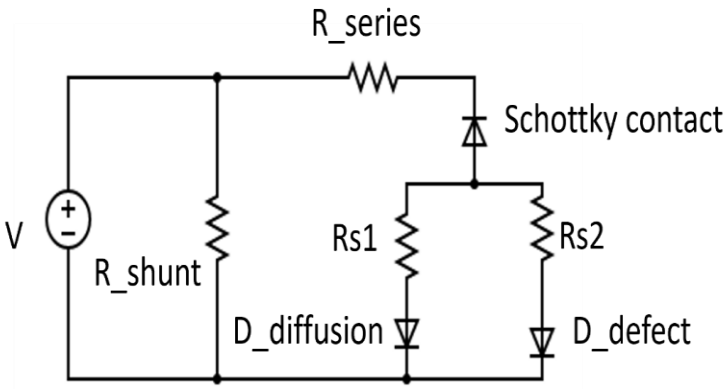

Figure 3.3: Circuit model 1 for I-V modeling

An excellent fit has been produced between the measured and modeled forward I-Vs at higher temperature (300~190 K) using this circuit model. However, an acceptable fit could not be established between assessed and computed I-V data at lower temperature (below 150 K). Even manipulation of circuit element parameters could not give us an acceptable fit. So, to emulate the circuit behavior properly, we must think out of the box. Following two figures clearly confirms the fact that this model can be applied to explain the current conduction mechanism of our device at temperatures up to 190 K.

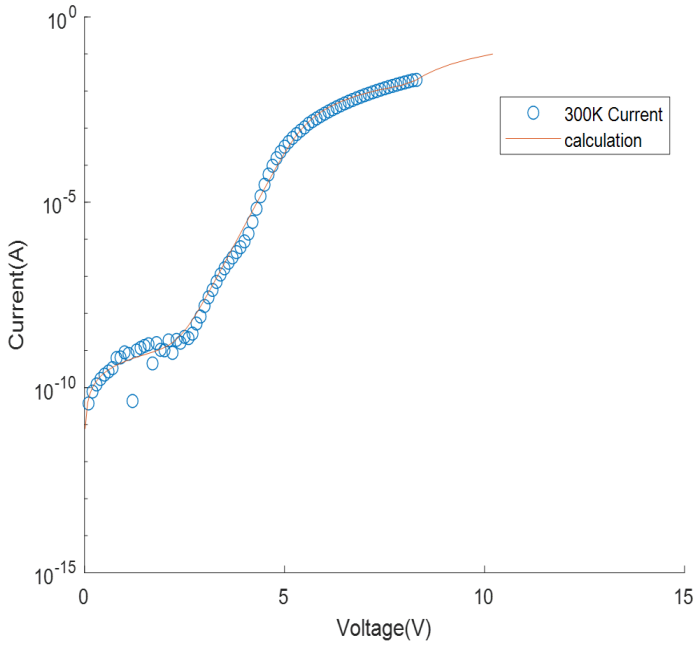

(a)

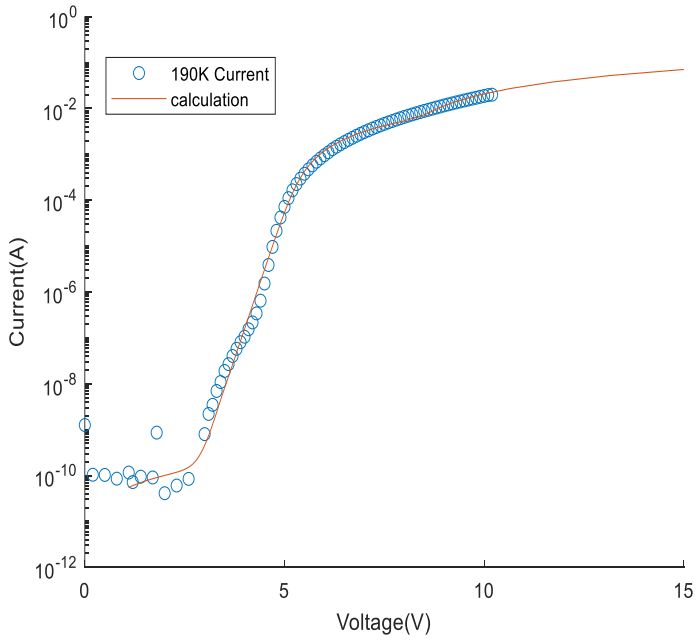

(b)

Figure 3.4: Experimental and simulated forward bias I-V characteristics of DUV photodiodes (a) At 300 K and (b) At 190 K.

The following table provides the summary of the parameters that are used for producing excellent fit.

Table 3.1: Summary of the parameters to emulate I-V behavior using model 1

Temp	R series	n Contact	Contact Leakage current (A)	Rs_1, (ohm)	Rs_2, (ohm)	Is_1, diffusion diode (A)	Is_2, defect diode (A)	Rshunt (ohm)
90 K	220	13.7	10e-27	3800	290	1e-4	1e-72	20e9
150 K	100	10.2	10e-22	750	50	10e-4	1e-45	50e9
190 K	70	9.2	70e-20	350	40	5e-9	1e-32	20e9
270 K	30	7.3	30e-17	150	60	5e-11	1e-26	20e8
300 K	14	7.3	9e-15	130	5	5e-12	1e-23	20e8

For space charge limited contact, we have used $I= V^2$. The main components are two diodes, diffusion and defect induced diodes. However, it can be seen from the table that, the parameters for generating fit at higher temperature look consistent with literature but for temperatures lower than~150 K, current through diffusion diode must be in the range of 1e-4 A to create somehow acceptable fit which is quite unphysical. Following figure shows the inconsistency in the fits using circuit model 1 for lower temperatures.

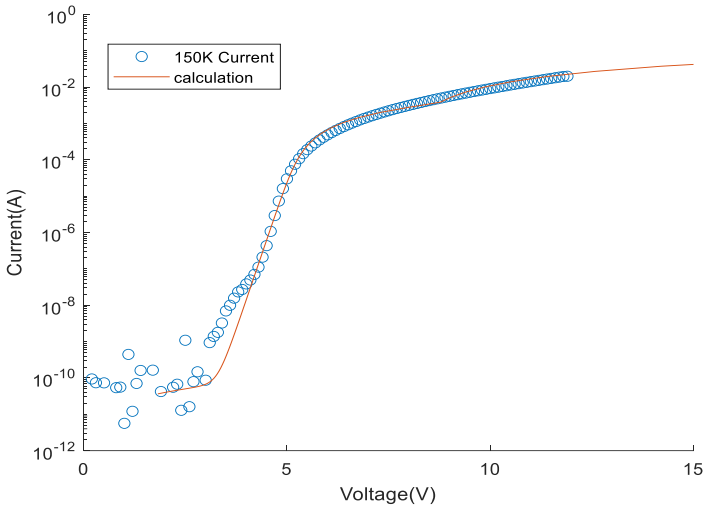

Figure 3.5: Discrepancy in the fits at lower temperature (150 K)

To solve the issue, we added a parallel resistor and checked the parameters whether it is consistent with the literature as well as our experimental data. By using MATLAB, we have tried producing a fit and this time the fits are more accurately generated. The model and the generated fits are showed in the following figures.

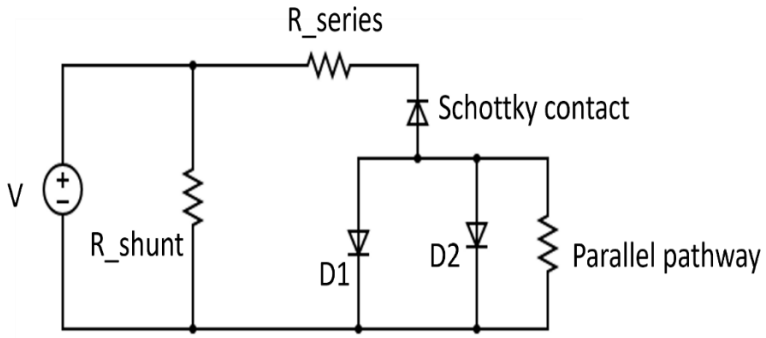

Figure 3.6: Circuit model 2 for I-V modeling

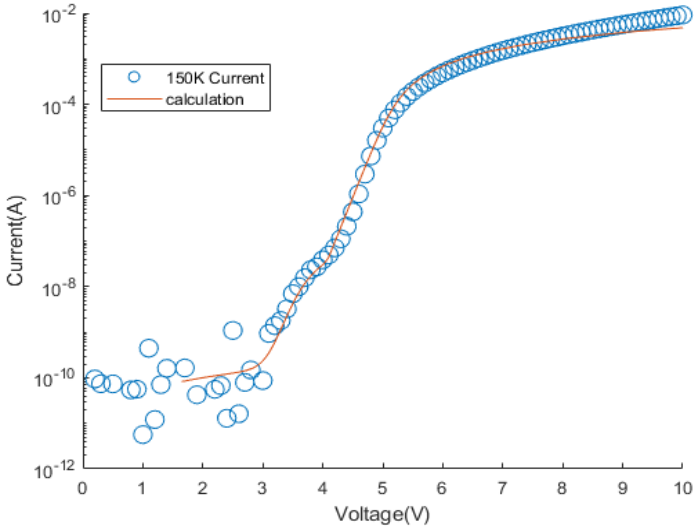

Figure 3.7: An acceptable fit generated using model 2
(At 150 K Temperature)

Table 3.2 provides us the parameters we got for generating the fits using model 2. This result is quite different than the values we got from previous fit generation.

Table 3.2: Summary of the parameters to emulate I-V behavior using model 2

Temp	R series	n Contact	Contact Leakage current (A)	Is_1, diffusion diode (A)	Is_2, defect diode (A)	R_parallel (ohm)	Rshunt (ohm)
90 K	2300	12.8	1e-25	4e-40	1e-72	1e8	80e9
150 K	900	9.2	10e-22	5e-20	1e-45	1e7	20e9
190 K	450	8.5	70e-20	5e-19	1e-32	1e7	20e9
270 K	200	6.8	30e-17	5e-17	1e-14	1e8	20e8
300 K	180	6.7	9e-15	4e-17	1e-12	1e8	20e8

We have found a downward trend of ideality factor with the increase in temperature. The shunt resistance also decreased at higher temperature fits. So, basically at lower temperature, open core threading dislocation defects (nano pipes) freeze out and conduction does not take place because of that. The following figure show the change in ideality factor as a function of by manipulating the circuit model parameters.

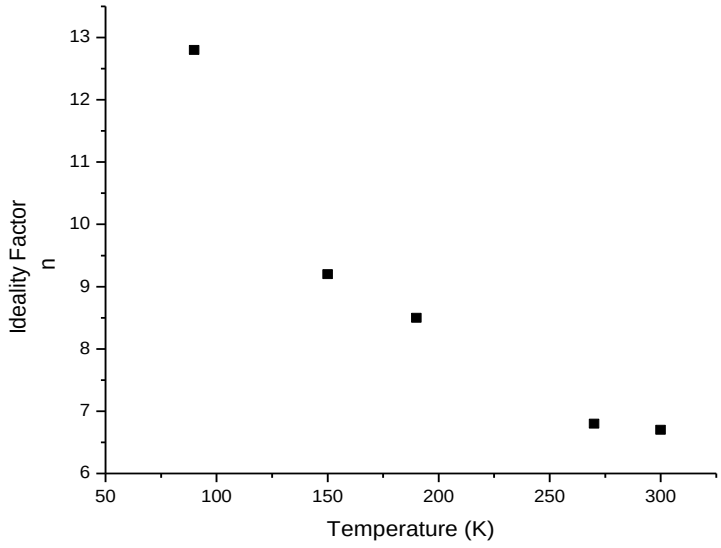

Figure 3.8: Downward trend of contact ideality factor with temperature increase

Two different circuit models are used to emulate the forward I-V characteristics of micropixel p-n diode. A simple two-diode circuit is used to check the accuracy of the model using MATLAB. While the circuit was able to accurately model the DUV-LED with a high density of nanopipes, it was unable to model the smaller leakage currents in the DUV-LED. The use of parallel resistor along with the diodes solved the discrepancy and helped us to perfectly explain the conduction mechanism due to nano-pipe freeze out mechanism.

CHAPTER 4

INCREASED DETECTIVITY ANALYSIS OF MICROPIXEL PHOTODIODES

The experiments outlined in chapter 2 revealed many fascinating and applicable properties of the sub 20 μm micropixel array AlGaN UV photodiodes. Some of the relevant findings will be repeated here with supplementary supporting data and assessment. It was demonstrated that we were in fact able to observe, quantize, and understand the behavior and some enhancements of the micropixel devices and comparison of the pixelated and reference stand-alone 90 μm devices through observation. The proposed architecture of the device shown in Figure 4.1 proved supreme in describing and understanding the observed behavior of the fabricated devices. The data and observations presented in this chapter will expand on various aspects of Figure 4.1 as they are analytically observed and verified.

4.1 BAND DIAGRAM

The band diagram is a diagram that plots various key electron energy levels as a function of some spatial dimension. This is very useful to understand the operation of many semiconductor devices and visualize the fluctuation in bands position. We have used 1D Poisson software to generate the band diagram of our epilayer structure. Figure 4.1 (b) represents the diagram that corresponds to the epilayer structure.

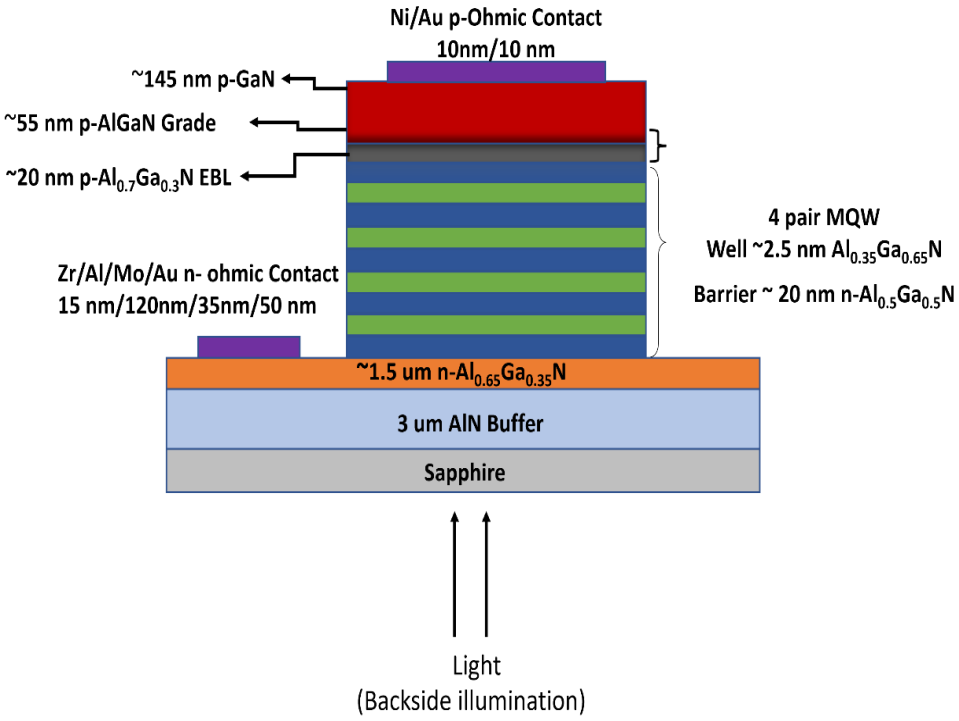

(a)

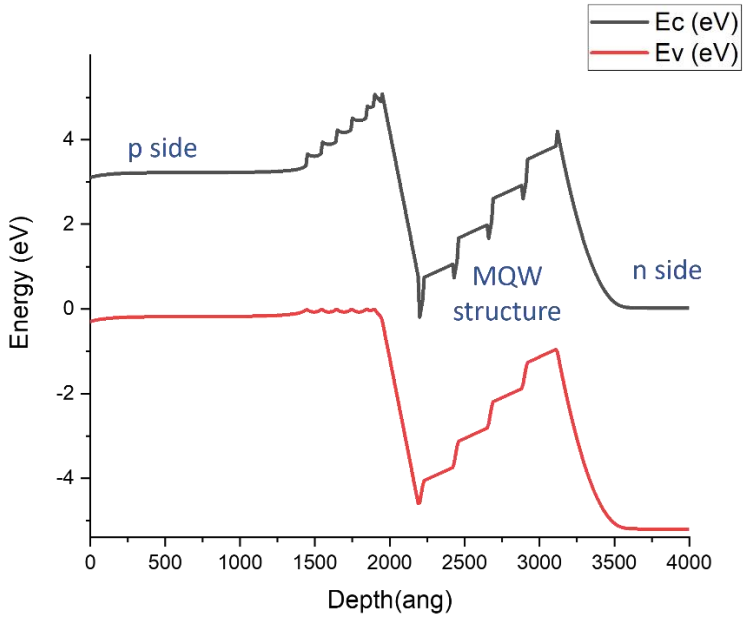

(b)

Figure 4.1: (a) Device Structure. (b) Band diagram corresponding to structure

In the above figure (4.1(b)), the top trace is the conduction band, and the lower trace is the valance band. Fermi level is 0 eV. In semiconductor-semiconductor and metal-semiconductor junctions, it is the Fermi energy levels that primarily determine the interaction and behavior at the junction of the two materials. Multiple quantum well region is the active region here and its fabricated to implement quantum effects in electronic and photonic structure. MQW basically consists of 4 pairs of $Al_{0.35}Ga_{0.65}N$ (Bandgap Energy, E_g= 4.345 eV) /$Al_{0.5}Ga_{0.5}N$ (E_g= 4.75 eV). The graded p layer can be distinguished clearly at the p side. The reason we used MQW structure is that it allows some degree of freedom in the design of the emitted wavelength through adjustment of the energy levels. 1D Poisson software basically produces values of energy levels within well by solving the Schrodinger equation. If we want to understand the carrier behavior at the junction, this band diagram of an epilayer structure surely provides us with important insights.

4.2 FORWARD AND REVERSE DARK I-V RESULTS

The I-V Characteristic Curves**,** which are known as Current-Voltage Characteristic Curves or simply I-V curves of an electrical device or component, are a set of graphical curves which are used to define its operation within an electrical circuit. As its name implies, I-V characteristic curves show the correlation between the current flowing through an electronic device and the applied voltage across its terminals.

I-V characteristic curves are generally used as a tool to determine and understand the basic parameters of a component or device, and which can also be used to mathematically model its performance within an electronic circuit. But as with most electronic devices, there are an unlimited number of I-V characteristic curves representing

the various inputs or parameters and as such we can display a family or group of curves on the same graph to represent the several values.

The forward and reverse I–V characteristics of our device are measured and shown in the following figures 4.2 and 4.3 respectively. The forward characteristic shown in figure 4.2 exhibits separate regions just like we have found in our previous studies [23]. We have taken measurements on arrays that have three distinct pixel sizes (5,10 and 15 μm) as well as on the reference 90 μm reference device. The ideality in the two areas where the current raises exponentially is defined as $n = (\partial \ln I/\partial V)/ V_{th}$, where $V_{th} = kT/q = 0.0259$ V is the thermal voltage at 300 K. Here, q is the electronic charge, k is the Boltzmann's constant, and T is the absolute temperature.

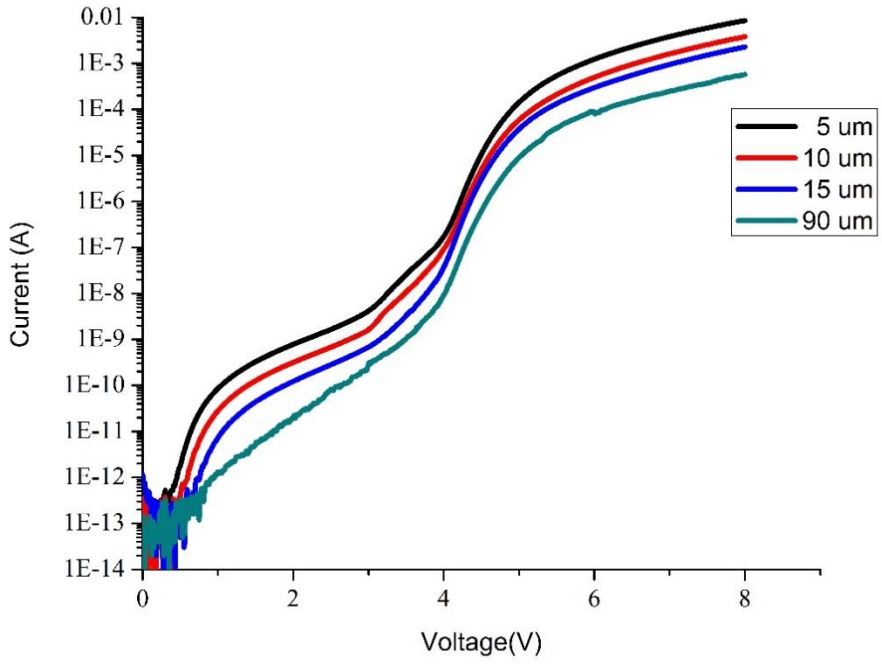

Figure 4.2: Forward I-V characteristics of photodetectors in the dark

If we carefully look at the above figure, we can find four distinct regions.

- For V<0.5 V, the current is very low (~0.1 pA) which is referred to device edge state at the mesa or can be attributed to noise.

- For V=0.5-1 V, the ideality is near 6 (~5.6) for all the subarray structures. This can be corresponding to 2 from the generation–recombination (G–R) current and 4 from the four MQWs embedded in the p–n junction. Each MQW structure behaves as a Schottky barrier in series with the entire structure, as described by Zhu et al [24]. This thing would be clearer if we look at the band structure where each QW has a triangular shape at the heterojunction interfaces which has a similar shape like Schottky barriers. On the other hand, if we focus on 90 μm reference device, its ideality is ~8 for the same voltage range. Some additional heterojunction interfaces could be produced in the p-n junction and that could be the justification for higher ideality factor.

- For V=4-5 V, the ideality for all four devices (including the reference one) is ~6. The carrier injection level increases with the current increase and screens out the barrier potential in each QW [24]. This could possibly be the reason of the lower ideality factor at higher voltages. The empty states in the MQW of reference photodiodes are filled and as a result, we have seen a lower n value.

- For V>5 V, the series resistance takes over and it dominates. We have seen four distinct values of series resistances. The values that we found for our devices with

5,10, 15 and 90 μm pixel sizes are 256, 561, 943 and 3720 Ω respectively. Micropixel devices have lower series resistances than the reference one. This resistance originates in the contacts, quasi-neutral regions, and spreading resistance as the current moves from the contacts to the active device area through the n+-AlGaN clad layer [20]. This series resistances in the pixelated devices are entirely sufficient for measuring low light levels, as photocurrents even in the milliampere range—corresponding to large deep ultraviolet light intensities—generate very small series voltage drops.

Figure 4.3 shows the dark I-V characteristics at reverse bias. Up to -10 V of reverse bias has been applied to all three arrays with different pixel sizes including the reference photodiode.

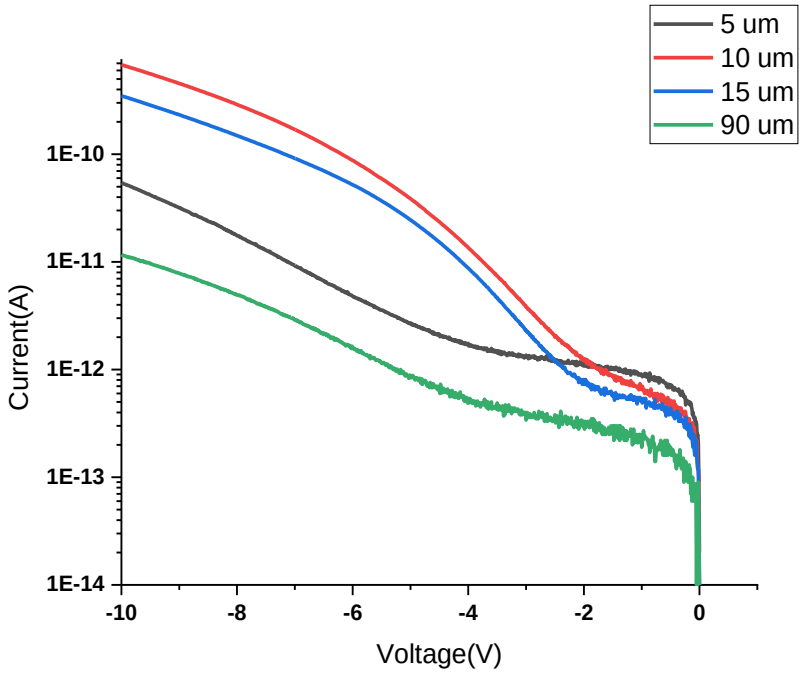

Figure 4.3: Reverse I-V characteristics of photodetectors in the dark

The above figure represents the reverse I-V characteristics graph which shows that, from 0 to -2 V, the dark current value for all four devices is nearly the same (~1 pA). As we further increase the reverse bias voltage, the dark current value increases rapidly for 10 and 15 μm pixel arrays whereas the increase in dark current is relatively flat for 5 μm pixel array and 90 μm reference device. It clearly epitomizes the fact that with 5 μm pixel sized device, we can achieve the same amount of reliability as our reference one. The shrinking in pixel size will not affect the dark current which is a very important parameter to consider during the design of any photodetector.

It is known that the higher the value of dark current, the larger the amount of noise would be. The major noises in the photodetectors are categorized as shot noise, thermal noise, and dark current noise. Dark current is basically a very small amount of electric current which flows when no photons are entering into the device. It is due to the random generation of electrons and holes within the depletion region. So, while shrinking the pixel size, one should keep in mind that the dark current which is an epitome of noise in the device shouldn't be affected. In our 5 μm pixelated device, the dark current increase from 0.2 pA to 50 pA as we increase the voltage from 0 to 10 V in the reverse direction. The value of increase is quite identical with our reference one. While our other pixelated devices (10 and 15 μm) do show some more leakage beyond -5 V.

The speed of the device is also dependent on reverse bias current. If we want to design a device that has a very large area, the possibility of getting a larger dark current is obvious if we choose one big device over our small micropixels. If the area is covered by micropixel arrays, the number of defects would be lower so as the dark current. Detecting

DUV light would be much easier as the generation component of the dark current would be minimized.

4.3 ILLUMINATED I-V RESULTS AND RESPONSIVITY CALCULATION

The action spectra of the device were measured over the range of 250-700 nm. When the device is illuminated, the electric field in the depletion region increases, which produces photocurrent. By illuminating the photodiode with sufficient optical radiation, we will be able to shift the dark I-V curve by the amount of photocurrent. We know that photodiode is basically a p-n junction that will convert light into electrical current. So, when photons are absorbed in the photodiode, the current is generated. Figure 4.4 surely gives us an insight into the current generation due to illumination.

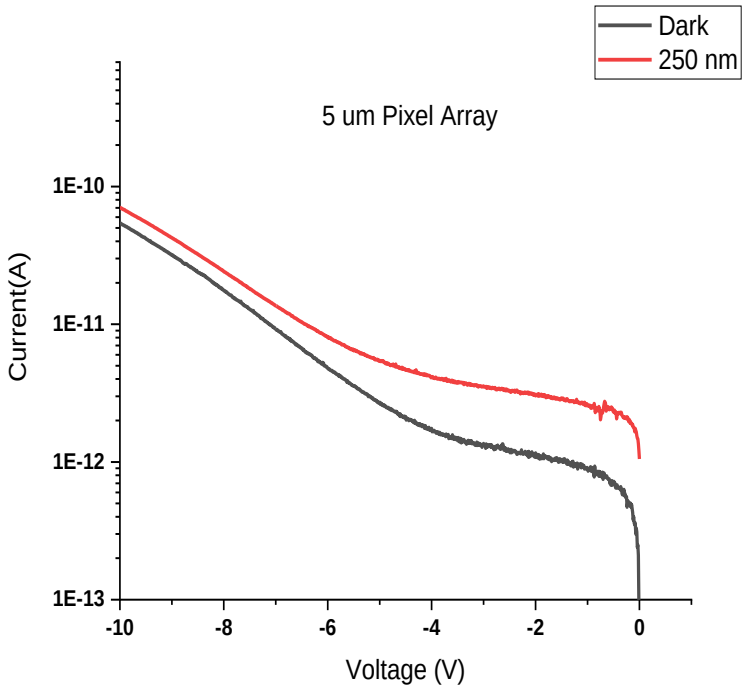

Figure 4.4: Dark and illuminated I-Vs for 5 µm pixel array

Figure 4.4 shows the shift in our I-V curve when our 5 µm pixel array has been irradiated by 250 nm light spectrum. The current level is above zero even when no voltage is applied to the device. By subtracting the dark current from the total current, we got our photocurrent value.

For measuring the photo response, we have irradiated the devices from back side. Illuminated I-V results are used to calculate responsivity R, which measures the input-output gain of the detector system. The responsivity of a photodiode or some other kind of photodetector is the ratio of generated photocurrent and incident (or sometimes absorbed) optical power (neglecting noise influences), determined in the linear region of response. In the case of photodiodes, the responsivity is typically highest in a wavelength region where the photon energy is somewhat above the band gap energy, and declining sharply in the region of the bandgap, where the absorption decreases. It can be calculated according to

$$R_\lambda = \frac{Ip}{P}\left(\frac{A}{W}\right) \tag{4.1}$$

Here,

I_p= Photocurrent (A)

P= incident optical Power (W)

While calculating the responsivity of our device we have tried normalizing by both junction area and cheap footprint area that has been calculated in chapter 2 and has been presented in table 2.1. However, Shrinking the pixel size requires more chip footprint area than the standard 90 µm device to fit all the pixels to get the same p-contact area. On the other hand, the junction area for micropixel based devices is much smaller than the

standalone device. In the following figures, we have presented responsivity graphs normalized by both kinds of areas. We have illustrated responsivity measurement at reverse bias voltage of 2 V as dark current is lower up to that voltage range.

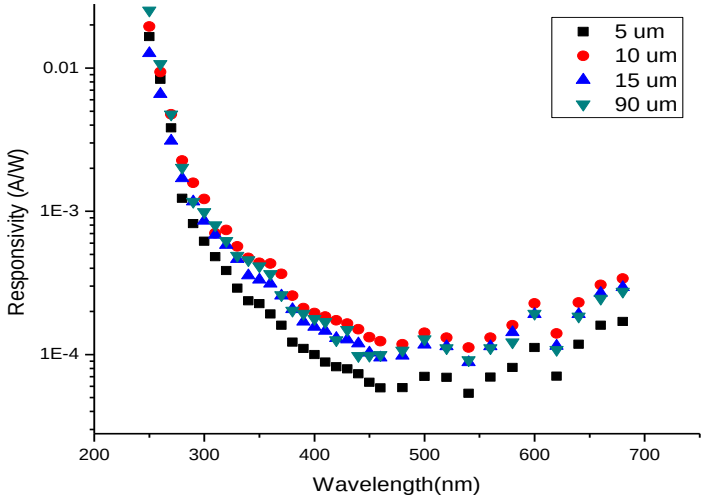

(a)

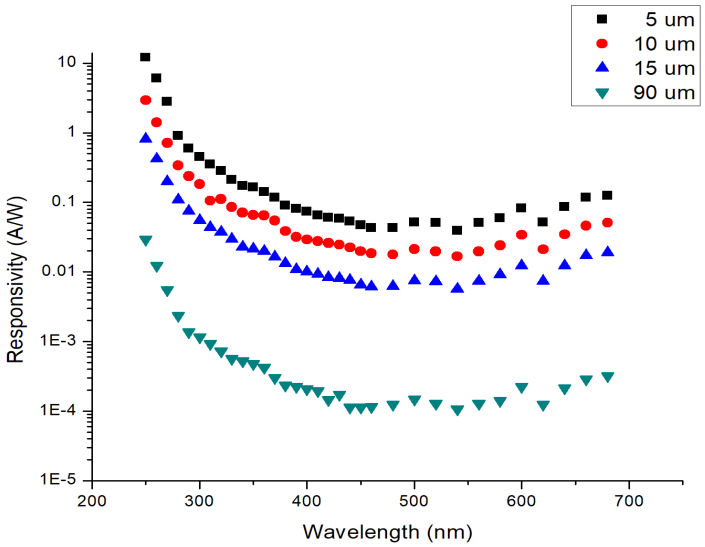

(b)

Figure 4.5: Responsivity Measurement at -2 V normalized by chip footprint area (a) and junction area (b)

Table 4.1 summarizes the peak responsivity values that we got from the above graphs.

Table 4.1: Peak Responsivity values for micropixel arrays

Pixel Size	**Peak Responsivity R @ 250 nm (A/W) Normalized by Junction Area**	**Peak Responsivity R @ 250 nm (A/W) Normalized by Chip footprint Area**
5 µm	12.1	1.67e-2
10 µm	2.92	2.62e-2
15 µm	0.811	1.62e-2
90 µm	0.0291	4.2e-2

As from the above responsivity values, it is confirmed to us that those values normalized by junction area of individual pixel don't make any sense. The values of responsivity for micropixel arrays are way above the reference one though their p contact area is the same for all. Another fact that proves the discrepancy in the calculation in terms of junction area is that the value of responsivity is above 1, which means that there's gain in our devices. But all devices are grown on the same structure and our photocurrent values don't indicate any sort of avalanche gain at -2 V. All these findings disregard the calculation of responsivity in terms of junction area. So actual measurement must be done by taking the chip footprint area as a reference area. This is the case where the responsivity values are identical and quite like our control structure and there is no gain as R values are way below 1. We have also calculated responsivity values other than -2 V. Photoconductive gain has been seen in 10 and 15 µm micropixel arrays as at higher voltages these arrays

have some leakage. As their dark current which is an indicator of any detector's performance is higher, the responsivity becomes greater than one and eventually it affects the detectivity of the devices. The following figure represents the responsivity graph taken at -10 V.

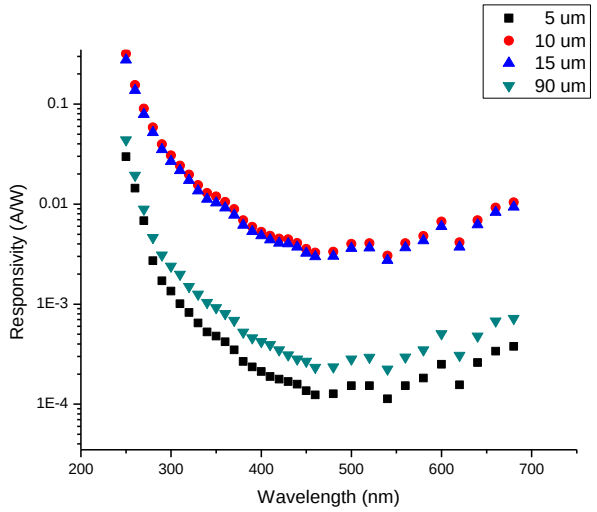

(a)

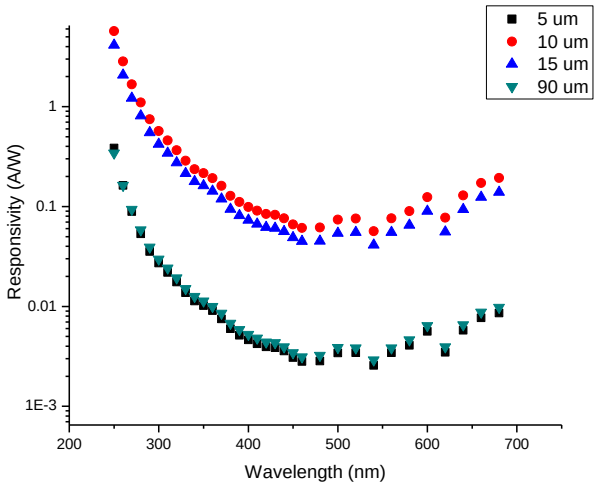

(b)

Figure 4.6: Responsivity Calculation for
(a) -5 V (b) -10 V applied bias

These devices show some responsivity at 0 V. Figure 4.7 depicts that fact. Though the values show very noisy behavior. So, for measuring the detectivity, a very small amount of reverse bias voltage should be applied to get noise free result.

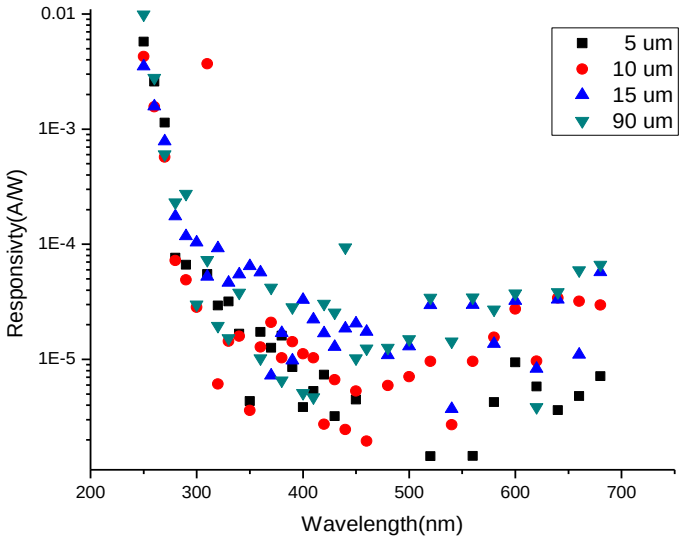

Figure 4.7: Responsivity Calculation at 0 V

4.4 INCREASED DETECTIVITY OF MICROPIXEL ARRAYS

As the photocurrent values are in the nA range, finding the speed or bandwidth of the device was somehow challenging for us. We have tried preamplifier for the amplification of our desired signal but could not be able to generate noise free signal. Literature shows that the recombination time of this kind of devices might be very short [24]. When designing a sensing circuit, one must know about two important parameters, series resistance and junction capacitance. Without this we cannot find the RC time constant of the complete operating circuit. For the 90 µm standalone device, the calculated resistance was 3720 ohm and the capacitance value was expected to be in the pF range, so theoretically we can expect an RC time constant in ns range. For micropixel array structures

we can expect that by reducing junction area we are lowering the value of junction capacitance, thus RC time constant should be lower which in turn increases the speed of the detector circuit. However, we cannot experimentally measure the operating speed because of the lower value of photocurrent.

So, by taking the sub 20 um pixel arrays, we are essentially trying to improve detectivity which is an important figure of merit to characterize the detector's performance. However, moving pixels apart additionally produces lateral current crowding which can be minimized by keeping interpixel spacing greater than minority carrier diffusion length but shorter than characteristic spreading length. High density packing of the small photosensitive pixels is used to minimize non-photo responsive areas. Our methodology is to modulate detectivity (D) by spreading out the active detection area. Detectivity (D) does affected by device area and can be specified as follows-

$$D = \frac{\sqrt{BA}}{NEP} = \frac{\sqrt{BA}}{\frac{i_{noise,white}}{R}} = \frac{R\sqrt{BA}}{\sqrt{S_{noise}\left(\frac{A^2}{Hz}\right)B(Hz)}} = \frac{R\sqrt{A}}{\sqrt{S_{noise}}} \qquad (4.2)$$

Here,

D= Detectivity (Jones)

A= Area of the photosensitive region of the detector (cm^2)

B= Bandwidth

NEP=Noise equivalent power

S_{noise}= Noise spectral density

R= Peak Responsivity of the device (A/W)

Noise spectral density is basically a combination of dark and thermal noise spectral density. Both dark and thermal noise is dependent on dark current. As from our

measurement we got quite similar amount of dark current and responsivity for all our structures, the only variable that will modulate our detectivity is the area of the photosensitive region of the detector. Our chip footprint area is increased almost 9x (from 1e-4 to 9e-4 cm^2) as we shrink our pixels from 90 µm to 5 µm to maintain the same p contact area. The values of detectivity that we got from our smallest micropixel arrays and control structures are 1.93419e12 and 1.62148e12 Jones respectively. So, almost 1.5x increase has been seen in detectivity although a huge increment of chip footprint area. Almost 9x chip footprint area doesn't affect the dark current which is an indicator of noise. On the other hand, smaller pixel size provides us with smaller junction area that's why the junction capacitance would be lower which in terms increases the operation speed of the device. Therefore, if we want to design a high-performance photo sensing device, choosing micropixel arrays over standalone structure provides us with low defects, low noise, and high-speed operation.

We have got almost 10% EQE which can be enhanced by the optimization of proper designing and growth condition.

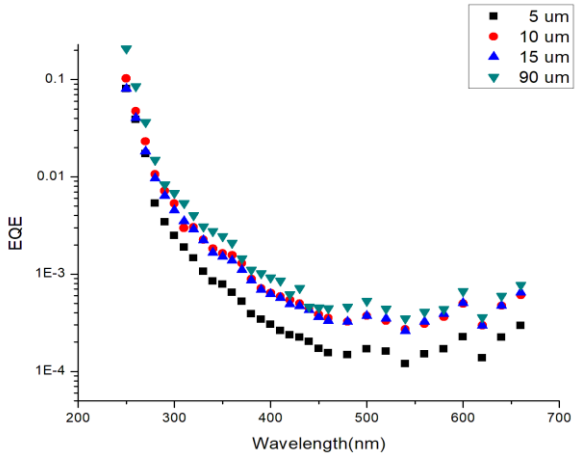

Figure 4.8: External quantum efficiency of photodiode arrays

4.5 CATHODOLUMINESCENCE (CL) IMAGING

We have obtained CL images of our structure to get a better insight into our design. CL imaging is basically a technique where a CL detector is attached with a scanning electron microscope to produce high resolution images of photoluminescence structure. We acquired CL spectra on mesa to determine at which wavelength we are going to take our image. We have used an accelerating voltage of 10 kV and taken images at MQW region wavelength which is almost 280 nm in our case.

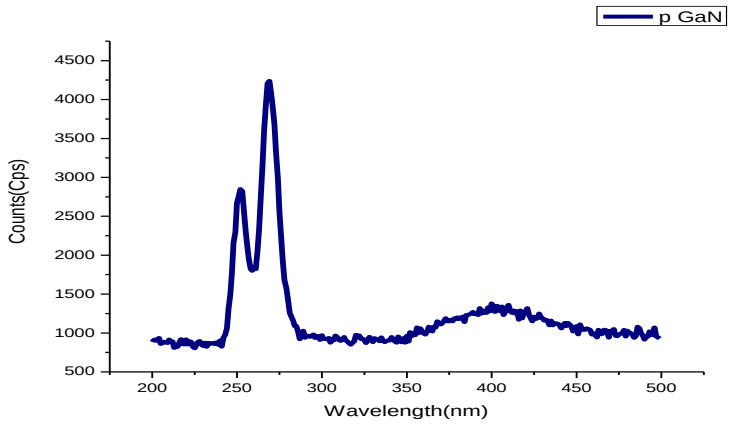

Figure 4.9: CL spectra taken on mesa structure. Highest peak at 280 nm which is basically MQW region wavelength

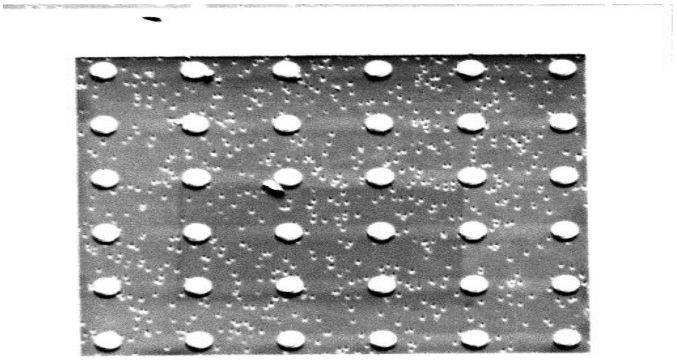

Figure 4.10: CL image of micropixel array taken at 280 nm wavelength

We have also tried imaging individual pixels at both SEI and AUX mode. We know that during CL electrons impacting on a photosensitive material causes the emission of photons. The following figure confirms the fact that the intensity of produced photon is maximum at the edge of the mesa and then it started decreasing. So, for designing a micropixel based detector circuit we must pay attention to interpixel spacing of individual detectors as well to get maximum output.

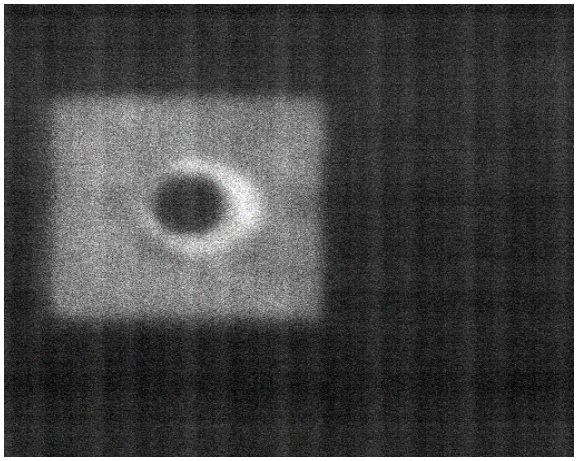

(a)

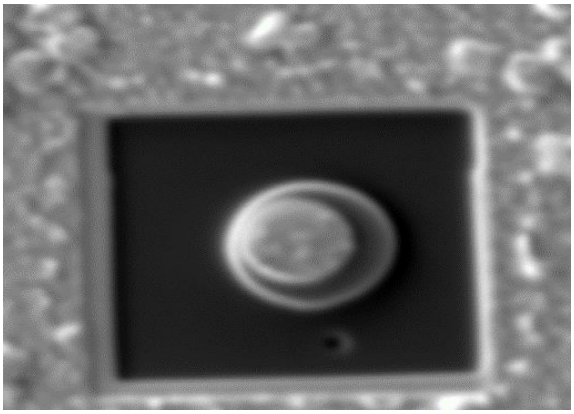

(b)

Figure 4.11: CL images of single 5 µm pixel taken at (a)SEI (b) AUX mode

4.6 SPACIAL PHOTOCURRENT MICROSCOPY (SPCM)

For a better understanding of the photogenerated charge transfer, we have employed SPCM (Spatial photocurrent microscopy) to spatially map the pixels. The SPCM scans utilized 444 nm incident light with the frequency of 31 Hz. If we look at the representative image, we can clearly identify a sharp increase in I_{ph} near the edge of the mesa.

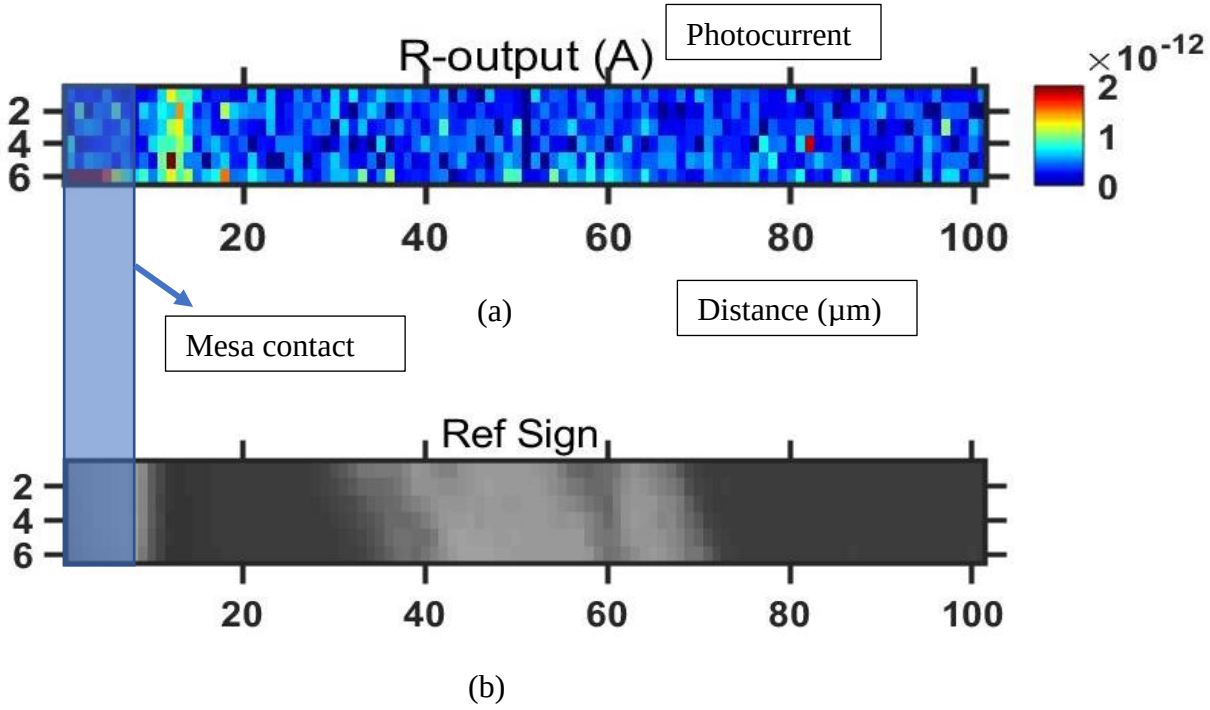

Figure 4.12: Representative SPCM (444 nm) (a) Photocurrent amplitude and (b) reflected images for -10 V reverse bias

The distance over which charge was collected and the insensitivity to applied bias of the decay length (Figure 4.12a) suggested that the Iph decay was not the minority carrier diffusion length which will fall apart at 0.1 µm but rather an increasing series resistance for excitation further away from the edge of the device. The average photocurrent that we

got after averaging 6 scanned lines can depict the current decay length which is almost 6 µm. Minority carrier diffusion length cannot be greater than 0.8 µm in our case if we consider a realistic recombination time of ~1 ns and a conservative estimate for the carrier mobility in AlGaN (~200 $cm^2V^{-1}s^{-1}$, which is between those of AlN and GaN)—implying a diffusion length of ~0.7 µm. So, there must be some transmission line mechanism creating this charge transport. The figure presented below gives us the current transfer length away from the mesa edge.

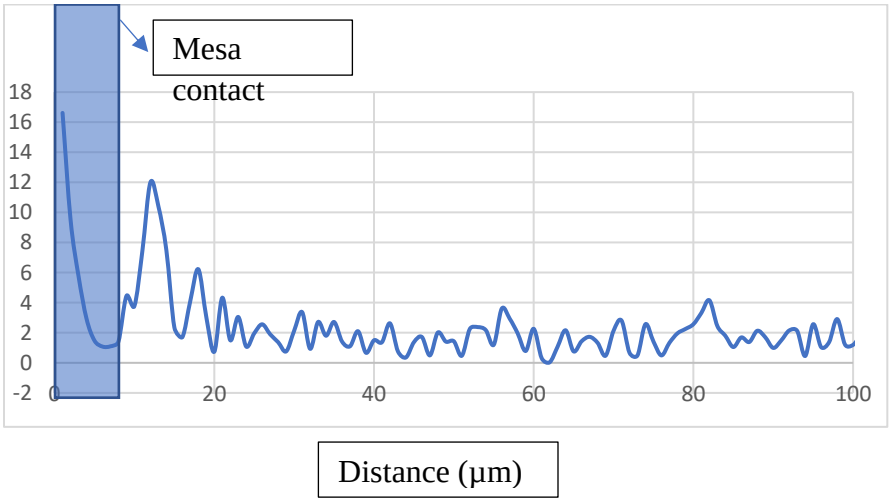

Figure 4.13: Average Photocurrent for 6 scanned lines

This photocurrent value is taken at AC. So, we believe that the current decay length for DC would be much higher as we observed in our previous works [25]. The interpixel distance between our micropixels is 5 µm. So, photocurrent can be collected up to 6 µm without any trouble. Nonetheless to say that this unique design provides us with a highly sensitive DUV detector which shows outstanding performance because of higher operating speed, reduced speed and improved detectivity.

CHAPTER 5

CONCLUSION AND FUTURE WORK

In this work, we have tried summarizing improvement in MQW based AlGaN UV photodiode's performance with necessary supporting documents. As we observed, 10x increase in device chip footprint area doesn't increase dark current, which is an indicator of noise. Therefore, for designing a large detector, this micropixel based geometry surely provides us with a better solution to fabricate devices with a higher figure of merit. Moreover, for better interpretation of the device's outcome, one must understand the underlying circuit mechanism which is creating this high-level result. The increase in light intensity at lower temperature surely makes us think of its proper clarification and Sandia team did came up with a better explanation. By emulating these models and showing the consistency between our experimental results and calculated fits, we basically tried to verify whether these models can give us a satisfactory explanation or not.

Although considerable progress has been made with AlGaN-based solar-blind UV PDs over the past two decades, the performances of these devices have yet to meet expectations, particularly with single photon detection. Obviously, the newly developed material and the improvement fabrication techniques provide a huge opportunity for the development of new generation UV detectors. Despite of that the biggest bottleneck in the development of AlGaN-based solar-blind UV PDs is the high-quality film epitaxy of high-Al-content AlGaN alloys.

Along with the development in high-quality film growth, a revolutionary design concept is further needed to explore versatile photodetectors toward the intelligent era beyond Moore's-law. Therefore, for the research of new concept UV photodetectors in the future, efforts should be made in the following three priority areas: materials, architectures, and applications [25].

Firstly, exploring suitable materials as an active layer is one of the fundamental steering forces for developing novel UV detectors. The detection and quantification of UV radiation at any wavelength can be realized nowadays by using alloy semiconductor fabrication techniques [26-30]. Therefore, to explore the diversity of materials for advanced UV photodetectors, the precise growth and assembly of nanostructures using energy band-gap engineering with low cost should be developed.

Secondly, based on handling and processing materials at the nanoscale with reliable reproducibility, plasmonic technology and energy bandgap engineering shall be used to fabricate various functional units (e.g., superlattice photoconductors), and further to that, advanced devices which could detect weak optical signals precisely at very high speed (e.g., germanium avalanche UV nano-photodetectors, tunneling devices, bipolar transistors, among others) [31].

Thirdly, from a practical perspective, self-powered UV photodetectors on flexible chips with multifunction have great potential to become regularly applied devices, because they cannot only be used as special 'electronic noses' to detect the humidity, toxic gas sensitivity while being powered by themselves, but also function as flexible batteries or hybrid supercapacitors.

Therefore, there is still plenty of room for the design of regenerative UV detectors in this flourishing age of optoelectronics. It is believed that future work in this field should continue to be concentrated on producing semiconductor nanostructures in a more controlled, conventional, and simpler way. Moreover, smart, sensible, portable, and multifunctional design concepts will bring more types of UV photodetectors out of the lab and help make them ready for real applications

REFERENCES

1. Liao, M.Y.; Sang, L.W.; Teraji, T.; Imura, M.; Alvarez, J.; Koide, Y. Comprehensive investigation of single crystal diamond deep-ultraviolet detectors. Jpn. J. Appl. Phys. 2012, 51, 090115:1–090115:7.

2. Chen, H., Liu, K., Hu, L., Al-Ghamdi, A. A., & Fang, X. (2015). New concept ultraviolet photodetectors. Materials Today, 18(9), 493-502.

3. Lin, C.H.; Liu, C.W. Metal-insulator-semiconductor photodetectors. Sensors 2010, 10, 8797–8826.

4. Monroy, E.; Omnes, F.; Calle, F. Wide-bandgap semiconductor ultraviolet photodetectors. Semicond. Sci. Technol. 2003, 18, R33–R51.

5. Omnes, F.; Monroy, E.; Munoz, E.; Reverchon, J.L. Wide bandgap UV photodetectors: A short review of devices and applications. Proc. SPIE 2007, 6473E, 1–15.

6. Toda, T.; Hata, M.; Nomura, Y.; Ueda, Y.; Sawada, M.; Shono, M. Operation at 700 °C of 6H-SiC UV sensor fabricated using N+ implantation. Jpn. J. Appl. Phys. 2004, 43, L27–L29.

7. Liao, M.Y.; Koide, Y.; Alvarez, J. Thermally stable visible-blind diamond photodiode using tungsten carbide Schottky contact. Appl. Phys. Lett. 2005, 87, 022105:1–022105:3.

8. Munoz, E. (Al,In,Ga)N-based photodetectors. Some materials issue. Phys. Stat. Sol. (b) 2007, 244, 2859–2877.

9. Monroy, E., Omnès, F., & Calle, F. J. S. S. (2003). Wide-bandgap semiconductor ultraviolet photodetectors. Semiconductor science and technology, 18(4), R33.

10. Khan, M. A. et al. High-responsivity photoconductive ultraviolet sensors based on insulating single-crystal GaN epilayers. Appl. Phys. Lett. 60, 2917–2919 (19).

11. Razeghi, M. III-nitride optoelectronic devices: from ultraviolet toward terahertz. IEEE Photonics J. 3, 263–267 (201).

12. Mohanbabu, A. & Mohankumar, N. Recessed Mg-doped P-type In0.2Ga0.8n cap gate AlGaN/GaN/AlGaN DH-HEMT for high breakdown and power electronics applications. In Proc. of 2016 International Conference on Inventive Computation Technologies. (IEEE, Coimbatore, 2016).

13. Sang, L., Liao, M., & Sumiya, M. (2013). A comprehensive review of semiconductor ultraviolet photodetectors: from thin film to one-dimensional nanostructures. *Sensors*, *13*(8), 10482-10518.

14. Pernot, C., Hirano, A., Iwaya, M., Detchprohm, T., Amano, H., & Akasaki, I. (1999). Low-intensity ultraviolet photodetectors based on AlGaN. *Japanese journal of applied physics*, *38*(5A), L487.

15. Cheng, Z., Koh, Y. R., Mamun, A., Shi, J., Bai, T., Huynh, K., ... & Graham, S. (2020). Experimental observation of high intrinsic thermal conductivity of AlN. *Physical Review Materials*, *4*(4), 044602.

16. Floyd, R., Gaevski, M., Alam, M. D., Islam, S., Hussain, K., Mamun, A., ... & Khan, A. (2020). An opto-thermal study of high brightness 280 nm emission AlGaN micropixel light-emitting diode arrays. *Applied Physics Express*, *14*(1), 014002.

17. Shatalov, M., Simin, G., Adivarahan, V., Chitnis, A., Wu, S., Pachipulusu, R., ... & Khan, M. A. (2002). Lateral current crowding in deep UV light emitting diodes over sapphire substrates. *Japanese journal of applied physics*, *41*(8R), 5083.

18. Graham, R., & Yu, D. (2013). Scanning photocurrent microscopy in semiconductor nanostructures. *Modern Physics Letters B*, *27*(25), 1330018.

19. Chitnis, A., Sun, J., Mandavilli, V., Pachipulusu, R., Wu, S., Gaevski, M., ... & Kuball, M. (2002). Self-heating effects at high pump currents in deep ultraviolet light-emitting diodes at 324 nm. *Applied Physics Letters*, *81*(18), 3491-3493.

20. Moseley, M. W., Allerman, A. A., Crawford, M. H., Wierer Jr, J. J., Smith, M. L., & Armstrong, A. M. (2015). Detection and modeling of leakage current in AlGaN-based deep ultraviolet light-emitting diodes. *Journal of Applied Physics*, *117*(9), 095301.

21. Hong, S. K., Yao, T., Kim, B. J., Yoon, S. Y., & Kim, T. I. (2000). Origin of hexagonal shaped etch pits formed in (0001) GaN films. *Applied Physics Letters*, *77*(1), 82-84.

22. Barker, B. G., Chava, V. S. N., Daniels, K. M., Chandrashekhar, M. V. S., & Greytak, A. B. (2017). Sub-bandgap response of graphene/SiC Schottky emitter bipolar phototransistor examined by scanning photocurrent microscopy. *2D Materials*, *5*(1), 011003.

23. Muhtadi, S., Hwang, S. M., Coleman, A. L., Lunev, A., Asif, F., Chava, V. S. N., ... & Khan, A. (2016). High-speed solar-blind UV photodetectors using high-Al content Al0. 64Ga0. 36N/Al0. 34Ga0. 66N multiple quantum wells. *Applied Physics Express*, *10*(1), 011004.

24. Zhu, D., Xu, J., Noemaun, A. N., Kim, J. K., Schubert, E. F., Crawford, M. H., & Koleske, D. D. (2009). The origin of the high diode-ideality factors in GaInN/GaN multiple quantum well light-emitting diodes. *Applied Physics Letters*, *94*(8), 081113.

25. Whitehead, R. F., de Mora, S. J., & Demers, S. (2000). Enhanced UV radiation—a new problem for the marine environment. *The effects of UV radiation in the marine environment*, *10*, 1-34.

26. Sang, L., Liao, M., & Sumiya, M. (2013). A comprehensive review of semiconductor ultraviolet photodetectors: from thin film to one-dimensional nanostructures. *Sensors*, *13*(8), 10482-10518.

27. Guo, Z., Zhao, D., Liu, Y., Shen, D., Zhang, J., & Li, B. (2008). Visible and ultraviolet light alternative photodetector based on ZnO nanowire/n-Si heterojunction. *Applied Physics Letters*, *93*(16), 163501.

28. Ju, Z. G., Shan, C. X., Jiang, D. Y., Zhang, J. Y., Yao, B., Zhao, D. X., ... & Fan, X. W. (2008). Mg x Zn 1− x O-based photodetectors covering the whole solar-blind spectrum range. *Applied Physics Letters*, *93*(17), 173505.

29. Fan, M. M., Liu, K. W., Chen, X., Zhang, Z. Z., Li, B. H., Zhao, H. F., & Shen, D. Z. (2015). Realization of cubic ZnMgO photodetectors for UVB applications. *Journal of Materials Chemistry C*, *3*(2), 313-317.

30. Wang, L. K., Ju, Z. G., Zhang, J. Y., Zheng, J., Shen, D. Z., Yao, B., ... & Shan, C. X. (2009). Single-crystalline cubic MgZnO films and their application in deep-ultraviolet optoelectronic devices. *Applied Physics Letters*, *95*(13), 131113.

31. Chen, H., Liu, K., Hu, L., Al-Ghamdi, A. A., & Fang, X. (2015). New concept ultraviolet photodetectors. *Materials Today*, *18*(9), 493-502.